THE METHOD OF FUNDAMENTAL SOLUTIONS FOR THE OSEEN STEADY-STATE VISCOUS FLOW PAST OBSTACLES OF KNOWN OR UNKNOWN SHAPES

ANDREAS KARAGEORGHIS AND DANIEL LESNIC

Abstract. In this paper, the steady-state Oseen viscous flow equations past a known or unknown obstacle are solved numerically using the method of fundamental solutions (MFS), which is free of meshes, singularities and numerical integrations. The direct problem is linear and well-posed, whereas the inverse problem is nonlinear and ill-posed. For the direct problem, the MFS computations of the fluid flow characteristics (velocity, pressure, drag and lift coefficients) are in very good agreement with the previously published results obtained using other methods for the Oseen flow past circular and elliptic cylinders, as well as past two circular cylinders. In the inverse obstacle problem the boundary data and the internal measurement of the fluid velocity are minimized using the MATLAB© optimization toolbox `lsqnonlin` routine. Regularization was found necessary in the case the measured data is contaminated with noise. Numerical results show accurate and stable reconstructions of various star-shaped obstacles of circular, bean or peanut cross-section.

1. Introduction

The equations of motion (Navier-Stokes equations) and continuity for an incompressible, Newtonian viscous fluid flow past an arbitrary finite body Ω, at steady-state in the absence of body forces can be written using Cartesian tensor notation as follows:

$$\frac{\partial \sigma_{jk}}{\partial x_k} - \varrho\, a_j = 0, \quad j = \overline{1,d}, \quad \text{in} \quad \mathbb{R}^d \backslash \overline{\Omega}, \tag{1.1}$$

$$\frac{\partial v_k}{\partial x_k} = 0 \quad \text{in} \quad \mathbb{R}^d \backslash \overline{\Omega}, \tag{1.2}$$

where d is the dimensional space, usually $d = 2$ or 3, σ_{jk} is the stress tensor, v_k are the fluid velocity components, ϱ is the fluid density and a_j are the acceleration components per unit mass given by

$$a_j = v_k \frac{\partial v_j}{\partial x_k}, \quad j = \overline{1,d}. \tag{1.3}$$

The stress tensor can be written in the form:

$$\sigma_{jk} = -p\, \delta_{jk} + 2\mu \varepsilon_{jk}, \tag{1.4}$$

Date: May 21, 2019.

2010 *Mathematics Subject Classification.* Primary 65N35; Secondary 65N21, 65N38.

Key words and phrases. method of fundamental solutions, Oseen flow, inverse problems.

where p is the pressure, δ_{jk} is the Kronecker delta tensor which is unity if $j = k$ and zero if $j \neq k$, μ is the Newtonian (constant) dynamic velocity and ε_{jk} is the rate of strain given by

$$\varepsilon_{jk} = \frac{1}{2}\left\{\frac{\partial v_j}{\partial x_k} + \frac{\partial v_k}{\partial x_j}\right\}. \tag{1.5}$$

The boundary conditions over $\partial\Omega = \partial\Omega_1 \cup \partial\Omega_2$ can be of Dirichlet type, i.e. prescribed velocity,

$$v_j = \widehat{v}_j \quad \text{on} \quad \partial\Omega_1, \quad j = \overline{1,d}, \tag{1.6}$$

and of Neumann type, i.e. prescribed stress force,

$$t_j = \widehat{t}_j \quad \text{on} \quad \partial\Omega_2, \quad j = \overline{1,d}, \tag{1.7}$$

where

$$t_j = \sigma_{jk}\, n_k, \quad j = \overline{1,d}, \tag{1.8}$$

is the stress force or force per unit area, and n_k are the unit outward normal vector components on $\partial\Omega$. Robin or free surface boundary conditions can also be considered but are not discussed herein.

Oseen's linearized version of equation (1.3) for the external flow past a body Ω with the uniform flow of velocity U_∞ at infinity in the positive x_1-direction, as shown in Figure 1, is obtained by replacing the velocity v_k in (1.3) with $+\mathrm{U}_\infty\,\delta_{1k}$ such that the momentum equation (1.1) becomes:

$$\frac{\partial \sigma_{jk}}{\partial x_k} - \varrho\,\mathrm{U}_\infty \frac{\partial v_j}{\partial x_1} = 0, \quad j = \overline{1,d}, \quad \text{in} \quad \mathbb{R}^d\backslash\overline{\Omega}. \tag{1.9}$$

Physically, Oseen's equations (1.9) are suitable approximations for the steady uniform flow of an incompressible viscous flow past obstacles of relatively low Reynolds number $Re = \dfrac{\mathrm{U}_\infty \ell}{\nu}$, where $\nu = \mu/\varrho$ is the kinematic viscosity and ℓ is a characteristic length of the obstacle (e.g. $\ell =$ diameter for a circular cylinder). Introducing (1.4) and (1.5) in (1.9) results in, [28],

$$\mu\nabla^2 \boldsymbol{v} - \nabla p - \varrho \mathrm{U}_\infty \frac{\partial \boldsymbol{v}}{\partial x_1} = 0 \quad \text{in} \quad \mathbb{R}^d\backslash\overline{\Omega}, \tag{1.10}$$

where $\boldsymbol{v} = (u_k)_{k=\overline{1,d}}$ is the fluid velocity. We can also rewrite the continuity equation (1.2) in the divergence-free form

$$\nabla \cdot \boldsymbol{v} = 0 \quad \text{in} \quad \mathbb{R}^d\backslash\overline{\Omega}. \tag{1.11}$$

The solution of (1.9), together with the continuity equation (1.2), the usual no-slip boundary condition $v_j = 0$ on $\partial\Omega$ for $j = \overline{1,d}$, and the infinity condition $v_j \to +\mathrm{U}_\infty\delta_{1j}$ for $j = \overline{1,d}$ at infinity, represents the perturbation to the uniform flow caused by the presence of the body. Alternatively, it is the flow field generated by the same body moving in the negative x_1-direction with uniform velocity $-\mathrm{U}_\infty\delta_{1j}$, $j = \overline{1,d}$, in a fluid otherwise at rest. The perturbation fluid velocity defined as

$$u_j = v_j - \mathrm{U}_\infty\delta_{1j}, \quad j = \overline{1,d}, \tag{1.12}$$

will also satisfy the Oseen flow equations (1.10) and (1.11) in the form

$$\mu\nabla^2\boldsymbol{u} - \nabla p - \varrho \mathrm{U}_\infty \frac{\partial \boldsymbol{u}}{\partial x_1} = 0 \quad \text{in} \quad \mathbb{R}^d\backslash\overline{\Omega}, \tag{1.13}$$

$$\nabla \cdot \boldsymbol{u} = 0 \quad \text{in} \quad \mathbb{R}^d\backslash\overline{\Omega}, \tag{1.14}$$

and the boundary and infinity conditions:

$$u_j = -\mathrm{U}_\infty\, \delta_{1j} \quad \text{on} \quad \partial\Omega, \quad j = \overline{1,d}, \tag{1.15}$$

$$u_j \to 0,\ p \to 0 \quad \text{at infinity}, \quad j = \overline{1,d}. \tag{1.16}$$

A boundary element method (BEM) for the Oseen flow problem (1.2), (1.9), (1.15) and (1.16) in two dimensions was developed by Bush [5]. We next discuss the method of fundamental solutions (MFS).

2. The method of fundamental solutions (MFS)

The MFS (which is free of meshes, singularities and numerical integrations) for the Stokes flow, i.e. $Re \ll 1$, neglecting the inertia in which the terms a_j in (1.1) are equal to zero, was developed in [2, 29] for direct problems and in [6] for inverse boundary condition linear problems. For Oseen flow, the MFS was developed by Yano and Kieda [28]. However, the MFS they propose requires the use of complex variables and is restricted to two dimensions. For axisymmetric and three-dimensional problems we refer to [27] and [23], respectively.

The fundamental solution of the Oseen equation in two dimensions is given by the matrix, see [5],

$$U_{11}(\boldsymbol{x},\boldsymbol{x}') = \frac{1}{2\pi\varrho\,\mathrm{U}_\infty}\left\{\kappa\,\mathrm{e}^{\kappa\,(x-x')}\left[K_0(\kappa\,r) + \frac{x-x'}{r}K_1(\kappa\,r)\right] - \frac{x-x'}{r^2}\right\},$$

$$U_{12}(\boldsymbol{x},\boldsymbol{x}') = U_{21}(\boldsymbol{x},\boldsymbol{x}') = -\frac{y-y'}{2\pi\varrho\,\mathrm{U}_\infty r}\left\{\frac{1}{r} - \kappa\,\mathrm{e}^{\kappa\,(x-x')}K_1(\kappa\,r)\right\},$$

$$U_{22}(\boldsymbol{x},\boldsymbol{x}') = \frac{1}{2\pi\varrho\,\mathrm{U}_\infty}\left\{\frac{x-x'}{r^2} + \kappa\,\mathrm{e}^{\kappa\,(x-x')}\left[K_0(\kappa\,r) - \frac{x-x'}{r}K_1(\kappa\,r)\right]\right\},$$

For the pressure, we also define

$$P_1(\boldsymbol{x},\boldsymbol{x}') = \frac{1}{2\pi}\frac{(x-x')}{r^2}, \qquad P_2(\boldsymbol{x},\boldsymbol{x}') = \frac{1}{2\pi}\frac{(y-y')}{r^2},$$

where $\boldsymbol{x} = (x,y)$, $\boldsymbol{x}' = (x',y')$, $r = |\boldsymbol{x}-\boldsymbol{x}'|$, $\kappa = \dfrac{\varrho\mathrm{U}_\infty}{2\mu}$, and K_0 and K_1 are the modified Bessel functions of the second kind of order zero and one, respectively.

In the MFS we seek an approximation in the form

$$u_i(\boldsymbol{x}) = \sum_{j=1}^{N}\left(\alpha_j U_{i1}(\boldsymbol{x},\boldsymbol{\xi}_j) + \beta_j U_{i2}(\boldsymbol{x},\boldsymbol{\xi}_j)\right), \quad i = 1,2, \quad \boldsymbol{x} \in \mathbb{R}^2\backslash\Omega, \tag{2.1}$$

where $\xi_j \in \Omega$ for $j = \overline{1,N}$ are the source points (or 'singularities'). The source points are taken to lie on an internal pseudo-boundary $\partial\Omega' \subset \Omega$ which is a contraction of the boundary $\partial\Omega$ with a contraction factor $\eta \in (0,1)$. The boundary conditions (1.15) on the perturbation fluid velocity components

$$u_1 = -\mathrm{U}_\infty, \quad u_2 = 0, \quad \text{on} \quad \partial\Omega \tag{2.2}$$

will be collocated at $M \geq N$ points on the boundary $\partial\Omega$ in order to determine the coefficients α_j, β_j for $j = \overline{1,N}$. The resulting linear system of $2M$ equations in $2N$ unknowns obtained by collocation equations (2.2) at $\boldsymbol{x}_i \in \partial\Omega$ for $i = \overline{1,M}$, namely,

$$u_k(\boldsymbol{x}_i) = \sum_{j=1}^{N} \left[\alpha_j U_{k1}(\boldsymbol{x}_i, \boldsymbol{\xi}_j) + \beta_j U_{k2}(\boldsymbol{x}_i, \boldsymbol{\xi}_j)\right], \quad i = \overline{1,M}, \ k = 1,2, \tag{2.3}$$

can be solved using Gaussian elimination if $M = N$ or a least squares method if $M > N$. However, as the numbers $M \geq N$ increase, or as the contraction factor $\eta > 0$ decreases, this system becomes more ill-conditioned and then the truncated singular value decomposition, see Ramachandran [24] or the Tikhonov regularization, can be employed. The convergence of the MFS expansions (2.1) and (2.3) can be justified by the denseness of the set

$$S_E(\partial\Omega, \partial\Omega') := \mathrm{span}\{\boldsymbol{U}_{(k)}(\boldsymbol{x} - \boldsymbol{\xi})|_{\boldsymbol{x}\in\partial\Omega}; \ \boldsymbol{\xi} \in \partial\Omega', \ k = 1,2\} \oplus \mathbb{R}^2 \ \text{ in } \ (H^{1/2}(\partial\Omega))^2,$$

and of the set

$$S(\Omega, \partial\Omega') := \mathrm{span}\{\boldsymbol{U}_{(k)}(\boldsymbol{x} - \boldsymbol{\xi})|_{\boldsymbol{x}\in\Omega}; \ \boldsymbol{\xi} \in \partial\Omega', \ k = 1,2\} \ \text{ in } \ (L^2(\Omega))^2,$$

where $\boldsymbol{U}_{(k)} = \boldsymbol{U}\boldsymbol{e}_k$ for $k = 1,2$ and $\boldsymbol{e}_1 = (1,0) = \boldsymbol{i}$ and $\boldsymbol{e}_2 = (0,1) = \boldsymbol{j}$. These results can be proved in a similar way to those in [2] for the Stokes system and using the analytic unique continuation property for Oseen's equations established in [8].

Similar considerations can be posed in three dimensions.

Based on (2.1) the least squares imposition of the boundary conditions (2.2) reads as minimizing

$$S(\boldsymbol{\alpha}, \boldsymbol{\beta}) = \sum_{i=1}^{M} \left(\left\{ \sum_{j=1}^{N} \left[\alpha_j U_{11}(\boldsymbol{x}_i, \boldsymbol{\xi}_j) + \beta_j U_{12}(\boldsymbol{x}_i, \boldsymbol{\xi}_j)\right] + \mathrm{U}_\infty \right\}^2 + \left\{ \sum_{j=1}^{N} \left[\alpha_j U_{21}(\boldsymbol{x}_i, \boldsymbol{\xi}_j) + \beta_j U_{22}(\boldsymbol{x}_i, \boldsymbol{\xi}_j)\right] \right\}^2 \right). \tag{2.4}$$

Defining the matrix

$$\begin{aligned}
Q_{ij} &= U_{11}(\boldsymbol{x}_i, \boldsymbol{\xi}_j), \quad i = \overline{1,M}, \ j = \overline{1,N}, \\
Q_{ij} &= U_{12}(\boldsymbol{x}_i, \boldsymbol{\xi}_{j-N}), \quad i = \overline{1,M}, \ j = \overline{N+1,2N}, \\
Q_{ij} &= U_{21}(\boldsymbol{x}_{i-M}, \boldsymbol{\xi}_j), \quad i = \overline{M+1,2M}, \ j = \overline{1,N}, \\
Q_{ij} &= U_{22}(\boldsymbol{x}_{i-M}, \boldsymbol{\xi}_{j-M}), \quad i = \overline{M+1,2M}, \ j = \overline{N+1,2N}, \\
\gamma_j &= \alpha_j, \quad j = \overline{1,N}, \quad \gamma_j = \beta_{j-N}, \quad j = \overline{N+1,2N},
\end{aligned}$$

$$b_i = -\mathrm{U}_\infty, \quad i = \overline{1, M}, \quad b_i = 0, \quad i = \overline{M+1, 2M},$$

the expression for S becomes

$$S(\boldsymbol{\gamma}) = ||Q\boldsymbol{\gamma} - \boldsymbol{b}||^2.$$

Minimizing S we obtain

$$\boldsymbol{\gamma} = \left(Q^T Q\right)^{-1} Q^T \boldsymbol{b}$$

where the superscript T denotes the transpose of a matrix.
Once the coefficients α_j and β_j for $j = \overline{1, N}$ have been computed, the fluid velocity in $\mathbb{R}^2\backslash\Omega$ can be obtained from equations (2.1) and (1.12). The pressure can also be obtained from

$$p(\boldsymbol{x}) = \sum_{j=1}^{N} \left[\alpha_j P_1(\boldsymbol{x}, \boldsymbol{\xi}_j) + \beta_j P_2(\boldsymbol{x}, \boldsymbol{\xi}_j)\right], \quad \boldsymbol{x} \in \mathbb{R}^2\backslash\Omega. \tag{2.5}$$

3. Calculation of the drag and lift coefficients

We shall be using the general formula for the total force per length in the direction perpendicular to the plane, $\boldsymbol{F} = (F_1, F_2) = (D_P + D_F, L_P + L_F)$, [25],

$$F_i = -\int_{\partial\Omega} p\, n_i\, ds + \mu \int_{\partial\Omega} \left[\frac{\partial u_i}{\partial x_1} n_1 + \frac{\partial u_i}{\partial x_2} n_2 + \frac{\partial u_1}{\partial x_i} n_1 + \frac{\partial u_2}{\partial x_i} n_2\right] ds, \quad i = 1, 2, \tag{3.1}$$

where $\boldsymbol{n} = (n_1, n_2)$ is the outward unit normal to the boundary $\partial\Omega$ of the obstacle Ω and $x_1 = x, x_2 = y$.

3.1. Flow past a circular cylinder.

In order to calculate the drag coefficient we use the formula,

$$C_D = \frac{1}{\varrho\, a\, \mathrm{U}_\infty^2} \left(D_P + D_F\right), \tag{3.2}$$

where, in the case of a circular cylinder of radius $a > 0$, we have that the pressure drag is

$$D_P = -\int_0^{2\pi} P(\vartheta)\, \cos\vartheta\; a d\vartheta, \tag{3.3}$$

where $P(\vartheta) := p(a\cos\vartheta, a\sin\vartheta)$, and the frictional drag is

$$D_F = \mu \int_0^{2\pi} \left(W_1(\vartheta)\, \cos\vartheta + W_2(\vartheta)\, \sin\vartheta\right)\; a d\vartheta = \mu \int_0^{2\pi} W(\vartheta)\, \sin\vartheta\; a d\vartheta, \tag{3.4}$$

where $W_\ell(\vartheta) := w_\ell(a\cos\vartheta, a\sin\vartheta)$, $\ell = 1, 2$, $W(\vartheta) := w(a\cos\vartheta, a\sin\vartheta)$ with

$$w_1(x, y) = 2\frac{\partial u_1}{\partial x}(x, y), \quad w_2(x, y) = \frac{\partial u_1}{\partial y}(x, y) + \frac{\partial u_2}{\partial x}(x, y)$$

and

$$w(x, y) = \frac{\partial u_1}{\partial y}(x, y) - \frac{\partial u_2}{\partial x}(x, y).$$

We can also consider the flow past two cylinders, see Figure 2(a). Note that in the case of flow past a single circular cylinder, we get that $D_P = D_F$, see [25, p.149]. Similarly, in order to calculate the lift coefficient we use the formula

$$C_L = \frac{1}{\varrho\, a\, \mathrm{U}_\infty^2}\left(L_P + L_F\right), \tag{3.5}$$

where, in the case of a circular cylinder, we have that the pressure lift is

$$L_P = -\int_0^{2\pi} P(\vartheta)\, \sin\vartheta\; a d\vartheta, \tag{3.6}$$

and the frictional drag is

$$L_F = \mu \int_0^{2\pi} \left(W_2(\vartheta)\, \cos\vartheta + W_3(\vartheta)\, \sin\vartheta\right)\; a d\vartheta = -\mu \int_0^{2\pi} W(\vartheta)\, \cos\vartheta\; a d\vartheta, \tag{3.7}$$

where $W_3(\vartheta) := w_3(a\cos\vartheta, a\sin\vartheta)$ with

$$w_3(x,y) = 2\frac{\partial u_2}{\partial y}(x,y).$$

3.2. **Flow past an elliptic cylinder.** In this case, we consider an elliptical cylinder with major and minor axes of lengths $2a$ and $2b$, respectively, with the major axis inclined at an angle ω to the horizontal, as shown in Figure 2(b). In this case, the coordinates of the ellipse are defined from the star shaped representation,

$$x = r(\vartheta)\cos\vartheta, \quad y = r(\vartheta)\sin\vartheta, \quad \vartheta \in [0, 2\pi), \tag{3.8}$$

where

$$r(\vartheta) = \frac{1}{\sqrt{\dfrac{\cos^2(\vartheta+\omega)}{a^2} + \dfrac{\sin^2(\vartheta+\omega)}{b^2}}}. \tag{3.9}$$

Moreover, the unit normal vector to the boundary is defined from

$$\boldsymbol{n}(\vartheta) = \frac{1}{\sqrt{r^2(\vartheta) + r'^2(\vartheta)}}\Big(r'(\vartheta)\sin\vartheta + r(\vartheta)\cos\vartheta,\; r(\vartheta)\sin\vartheta - r'(\vartheta)\cos\vartheta\Big) \tag{3.10}$$

and $ds = \sqrt{r^2(\vartheta) + r'^2(\vartheta)}\, d\vartheta$. Thus, from equation (3.1) for $i = 1$, we get

$$D_P = -\int_0^{2\pi} P(\vartheta)\, n_1(\vartheta)\sqrt{r^2(\vartheta) + r'^2(\vartheta)}\, d\vartheta = -\int_0^{2\pi} P(\vartheta)\; \left(r'(\vartheta)\sin(\vartheta) + r(\vartheta)\cos(\vartheta)\right)\; d\vartheta \tag{3.11}$$

where $P(\vartheta) := p(r(\vartheta)\cos\vartheta, r(\vartheta)\sin\vartheta)$, and

$$D_F = \int_0^{2\pi} \left(W_1(\vartheta)\, n_1(\vartheta) + W_2(\vartheta)\, n_2(\vartheta)\right)\; \sqrt{r^2(\vartheta) + r'^2(\vartheta)}\, d\vartheta$$

$$= \int_0^{2\pi} \left(W_1(\vartheta)\; \left(r'(\vartheta)\sin(\vartheta) + r(\vartheta)\cos(\vartheta)\right) + W_2(\vartheta)\; \left(r(\vartheta)\sin\vartheta - r'(\vartheta)\cos\vartheta\right)\right)\; d\vartheta, \tag{3.12}$$

where $W_\ell(\vartheta) := w_\ell(r(\vartheta)\cos\vartheta, r(\vartheta)\sin\vartheta)$, $\ell = 1, 2$, and $W(\vartheta) := w(r(\vartheta)\cos\vartheta, r(\vartheta)\sin\vartheta)$. Also, the pressure lift is

$$L_P = -\int_0^{2\pi} P(\vartheta)\, n_2(\vartheta)\, \sqrt{r^2(\vartheta) + r'^2(\vartheta)}\, d\vartheta = -\int_0^{2\pi} P(\vartheta)\ (r(\vartheta)\sin\vartheta - r'(\vartheta)\cos\vartheta)\ d\vartheta \quad (3.13)$$

and the frictional drag is

$$L_F = \int_0^{2\pi} (W_2(\vartheta)\, n_1(\vartheta) + W_3(\vartheta)\, n_2(\vartheta))\ \sqrt{r^2(\vartheta) + r'^2(\vartheta)}\, d\vartheta,$$

$$= \int_0^{2\pi} (W_2(\vartheta)\ (r'(\vartheta)\sin(\vartheta) + r(\vartheta)\cos(\vartheta)) + W_3(\vartheta)\ (r(\vartheta)\sin\vartheta - r'(\vartheta)\cos\vartheta))\ d\vartheta, \quad (3.14)$$

where $W_3(\vartheta) := w_3(r(\vartheta)\cos\vartheta, r(\vartheta)\sin\vartheta)$. The drag and lift coefficients are obtained from (3.2) and (3.5), respectively.

In the above, we approximate the integrals using the trapezoidal rule

$$\int_0^{2\pi} \mathcal{P}(\vartheta)\ d\vartheta \approx \frac{2\pi}{\mathcal{M}} \left\{ \frac{1}{2}\mathcal{P}_0 + \mathcal{P}_1 + \ldots + \mathcal{P}_{\mathcal{M}-1} + \frac{1}{2}\mathcal{P}_{\mathcal{M}} \right\}, \quad (3.15)$$

where $\mathcal{P}_i = \mathcal{P}(2\pi i/\mathcal{M})$ for $i = \overline{0, \mathcal{M}}$. In the numerical experiments we chose $\mathcal{M} = 400$.

4. Numerical examples for the direct problem

4.1. **Example 1: A single circular cylinder.** We consider the Oseen fluid flow past a single circular cylinder of radius a in the positive x_1-direction, as shown in Figure 1. We chose the radius of the disk to be $a = 1$ and took $\varrho = 1, \mu = 1$. For various values of the speed U_∞, the corresponding Reynolds numbers are defined as $Re = \dfrac{2\mathrm{U}_\infty a}{\nu}$. The collocation and source points $(\boldsymbol{x}_i)_{i=\overline{1,M}}$ and $\left(\boldsymbol{\xi}_j\right)_{j=\overline{1,N}}$ were spread uniformly on the boundaries of the circle $\partial\Omega$ (of radius a) and of the contracted circle $\partial\Omega'$ (of radius ηa). In Table 1 we present the values of the drag coefficient C_D for various numbers of MFS degrees of freedom and $\eta = 0.8$. Clearly, as M and N increase these values converge. These converged values are in excellent agreement with the values previously reported in [5, 25] (and also [20, 26]), see Table 2.
In the subsequent numerical experiments of this subsection we took $M = 196, N = 148$ and $\eta = 0.8$.
The velocity vectors and pressure contours for $Re = 1$ are presented in Figure 3. We have also computed the perturbation fluid velocity $u_1(x_1, 0)$ for $|x_1| > a$ on the line of symmetry ahead and behind the cylinder, as a function of the distance from the centre of the cylinder, namely $\dfrac{(|x_1| - a)}{a}$, for various Reynolds numbers. The results shown in Figure 4 are in excellent agreement with Figure 2 of [5].

TABLE 1. The drag coefficient C_D obtained using the MFS with various numbers of degrees of freedom M and N for the Oseen flow past a circular cylinder of unit radius $a = 1$ at various Reynolds numbers Re.

Re	$M = 13, N = 10$	$M = 25, N = 19$	$M = 49, N = 37$	$M = 98, N = 74$	$M = 196, N = 148$
0.4	21.2519	21.2529	21.2527	21.2527	21.2527
1	11.8556	11.8571	11.8569	11.8569	11.8569
2	8.0805	8.0850	8.0847	8.0847	8.0847
3	6.6274	6.6366	6.6362	6.6362	6.6362
4	5.8282	5.8421	5.8416	5.8416	5.8416
6	4.9484	4.9699	4.9691	4.9691	4.9691
8	4.4597	4.4883	4.4869	4.4869	4.4869
10	4.1421	4.1774	4.1751	4.1751	4.1751

TABLE 2. The drag coefficient C_D obtained using the MFS with $M = 196, N = 148$ and $\eta = 0.8$, for the Oseen flow past a circular cylinder of unit radius $a = 1$ at various Reynolds numbers Re, in comparison with the results previously reported in the literature.

Re	C_D Bush [5]	C_D Eq. (20) in [5]	C_D [25]	C_D current
0.4	21.242	21.25	21.26	21.2527
1	11.849	11.86	11.86	11.8569
2	8.078	8.15	8.08	8.0847
3	6.630		6.636	6.6362
4	5.836		5.84	5.8416
6	4.964			4.9691
8	4.482		4.48	4.4869
10	4.170			4.1751

4.2. **Example 2: Two equal circular cylinders separated by a distance.** We consider the flow past two circular cylinders C_1 and C_2 of radius 1 separated by a distance $h = 20$, where the line joining the centres of the two cylinders makes an angle ω with the horizontal as shown in Figure 2(a). This problem was first considered in [9], see also [5, 28]. In our numerical experiments we took $M = 196, N = 148$ and $\eta = 0.8$ for each cylinder. In Figure 5(a) we present the ratio C_D/C_D^* versus the Reynolds number Re for various angles ω, where C_D is the calculated drag coefficient on cylinder C_1, and C_D^* is the drag coefficient calculated for a single cylinder using the formula (20) from [5]. In Figure 5(b) we present the lift coefficient C_L on the cylinder C_1 versus the Reynolds number Re for various angles ω. The results of both figures are in excellent agreement with the corresponding results in [5, 9, 28].

4.3. **Example 3: Elliptic cylinder.** We next consider the flow past an elliptic cylinder with major axis length $2a$ and minor axis length $2b$, with the major axis inclined at an angle ω to the horizontal as shown in Figure 2(b). The thickness of the ellipse is defined by the ratio $t = b/a$. In

our numerical experiments we took $a = 1$, $M = 196, N = 148$ and $\eta = 0.8$ for the case $t = 0.5$. For the case $t = 0.1$ we took $\eta = 0.1$ and a special distribution of the collocation and source points to avoid concentration near the ends of the minor axis. In Figures 6(a) and 6(b), we present the drag and lift coefficients C_D and C_L, respectively, for Re=1 (where $Re = 2aU_\infty/\nu$), $t = 0.5$ and 0.1. These results are in excellent agreement with the results of [5, 12].

5. Inverse obstacle problem

In the previous sections we were concerned with the formulation and solution of the direct problem of the Oseen flow past an arbitrary obstacle Ω. In this section, we formulate and solve numerically the inverse problem of determining the shape of a cylindrical obstacle immersed in an Oseen steady flow from the knowledge of the fluid velocity on some curve (usually closed, but it can also be only an arc in case of limited aperture) outside the obstacle. This inverse problem was previously analysed in [21] where the uniqueness of the star-shaped obstacle (centred at the origin) was established and a method based on the singular single layer potential combined with a regularized Newton iteration scheme were numerically implemented. In our investigation we shall use the MFS [16], which is meshless and non-singular, for approximating the solution for the perturbation fluid velocity by (2.1) combined with a nonlinear regularized least-squares minimization for detecting the radial polar coordinate $0 < r(\vartheta) \leq r_{\max}$ for $\vartheta \in [0, 2\pi)$ and $r_{\max} > 0$ an a priori given upper size, parametrising the unknown star-shaped obstacle (with respect to the origin):

$$\Omega = \{r(\vartheta)\,(\cos(\vartheta), \sin(\vartheta)) \mid \vartheta \in [0, 2\pi)\}\,. \tag{5.1}$$

In this case, taking $M = N$, we collocate (2.3) at the boundary collocation points

$$\boldsymbol{x}_i = (r_i \cos(\vartheta_i), r_i \sin(\vartheta_i))\,,\ i = \overline{1, N}, \tag{5.2}$$

where $r_i = r(\vartheta_i),\ \vartheta_i = 2\pi(i-1)/N$ for $i = \overline{1, N}$ with the associated sources

$$\boldsymbol{\xi}_i = (\eta\, r_i \cos(\vartheta_i), \eta\, r_i \sin(\vartheta_i))\,,\ i = \overline{1, N}. \tag{5.3}$$

The inverse flow problem and its MFS combined minimization procedure have similarities with the inverse scattering by soft obstacles previously treated by the authors in [15]. However, we remark that in comparison to the acoustic scattering problem, in the current fluid flow obstacle formulation there is no *a priori* bound on the size of the obstacle required for the uniqueness of its reconstruction [21]. In this formulation, the perturbed velocity $\boldsymbol{u}$ and the obstacle (5.1) need to be reconstructed by solving the mathematical problem given by equations (1.13)-(1.16) and the extra velocity measurement

$$\boldsymbol{u} = \boldsymbol{\varphi} \quad \text{on} \quad \Gamma, \tag{5.4}$$

where $\boldsymbol{\varphi}$ is a given function and Γ is a closed circular or box frame boundary, (or, in case of remote sensing, an aperture of it), placed at sufficiently large distances to ensure that it contains the unknown obstacle, e.g. far upstream/downstream and on the banks of a flowing river containing the immersed obstacle to be detected. Practically, the fluid velocity (5.4) is measured using flow meters installed in the fluid. As such, their intrusiveness may disturb the true flow around the obstacle, especially if the measurement curve Γ is situated in the proximity of the obstacle Ω

whose position in the fluid is unknown. On the other hand, the closer the measurement curve Γ is to $\partial\Omega$, the more information on reconstructing the obstacle Ω is contained in (5.4). In this numerical study, we neglect any errors in the fluid flow model caused by the flow meters presence, but we do take into account the noisy errors in the fluid velocity measurement (5.4), as described in (6.1).

Taking Γ to be a curve situated outside the disk $B(\mathbf{0}; r_{\max})$, usually a circle (or an arc of it) of radius $R_1 > r_{\max}$, and collocating (5.4) at L distinct points $(\boldsymbol{x}_{\ell+N})_{\ell=\overline{1,L}} \subset \Gamma$ (say uniformly distributed) results in $2L$ equations

$$\varphi_k(\boldsymbol{x}_{\ell+N}) = \sum_{j=1}^{N} \left[\alpha_j U_{k1}(\boldsymbol{x}_{\ell+N}, \boldsymbol{\xi}_j) + \beta_j U_{k2}(\boldsymbol{x}_{\ell+N}, \boldsymbol{\xi}_j)\right], \quad \ell = \overline{1,L},\ k = 1,2. \tag{5.5}$$

The density of the measurement points $(\boldsymbol{x}_{\ell+N})_{\ell=\overline{1,L}}$ on Γ, (which additionally cluster in case of a limited aperture), depends on the complexity (5.1) of the star-shaped obstacle Ω to be reconstructed. Altogether, expressions (2.3) (with $M = N$) and (5.4) yield $2N + 2L$ nonlinear algebraic equations in $3N + 1$ unknowns, namely, the MFS coefficients $\boldsymbol{\alpha} = (\alpha_j)_{j=\overline{1,N}}$, $\boldsymbol{\beta} = (\beta_j)_{j=\overline{1,N}}$, $\boldsymbol{r} = (r_i)_{i=\overline{1,N}}$ and we also treat η as an unknown (see [17]). Taking $2L > N$, we solve this system in a regularized least-squares sense given by

$$\begin{aligned} T_{\lambda_1,\lambda_2}(\boldsymbol{\alpha}, \boldsymbol{\beta}, \boldsymbol{r}, \eta) &:= S(\boldsymbol{\alpha}, \boldsymbol{\beta}, \boldsymbol{r}, \eta) + \lambda_1 \sum_{j=1}^{N} \left(\alpha_j^2 + \beta_j^2\right) + \lambda_2 \sum_{\ell=2}^{N} (r_\ell - r_{\ell-1})^2 \\ &+ \sum_{\ell=1}^{L} \left(\left\{ \sum_{j=1}^{N} \left[\alpha_j U_{11}(\boldsymbol{x}_{\ell+N}, \boldsymbol{\xi}_j) + \beta_j U_{12}(\boldsymbol{x}_{\ell+N}, \boldsymbol{\xi}_j)\right] - \varphi_1(\boldsymbol{x}_{\ell+N}) \right\}^2 \right. \\ &\left. + \left\{ \sum_{j=1}^{N} \left[\alpha_j U_{21}(\boldsymbol{x}_{\ell+N}, \boldsymbol{\xi}_j) + \beta_j U_{22}(\boldsymbol{x}_{\ell+N}, \boldsymbol{\xi}_j)\right] - \varphi_2(\boldsymbol{x}_{\ell+N}) \right\}^2 \right), \end{aligned} \tag{5.6}$$

where in the expression (2.4) defining S, the arguments $(\boldsymbol{x}_i)_{i=\overline{1,N}}$ depend on $\boldsymbol{r}$, as given by (5.2), and $\left(\boldsymbol{\xi}_j\right)_{j=\overline{1,N}}$ depend on $\boldsymbol{r}$ and η, as given by (5.3). Also, $\lambda_1 \geq 0$ and $\lambda_2 \geq 0$ are regularization parameters penalising the ill-conditioning of the MFS spectral representation (2.1) and the C^1-smoothness of the boundary $\partial\Omega$ of the obstacle Ω, respectively. These regularization terms are needed in order to stabilise the solution of the inverse and ill-posed obstacle problem under investigation in this section. We postpone the discussion of their choices to the next section where numerical results will be presented.

The minimization of the nonlinear functional (5.6) is performed subject to the simple bounds on the variables

$$-10^5 \leq \alpha_j \leq 10^5,\ -10^5 \leq \beta_j \leq 10^5,\ j = \overline{1,N},\ 0.1 \leq \eta \leq 0.99,\ r_{\min} \leq r_\ell \leq r_{\max},\ \ell = \overline{1,N}, \tag{5.7}$$

where $r_{\min}$ and $r_{\max}$ are lower and upper bounds on the size of the obstacle to be prescribed. This is accomplished using the MATLAB© [22] optimization toolbox routine `lsqnonlin`, which solves

nonlinear least squares problems using either a subspace trust region method or the Levenberg-Marquardt algorithm. The gradient of (5.6) does not need to be supplied by the user and `lsqnonlin` offers the option of imposing lower and upper bounds on the elements of the vector of unknowns $\boldsymbol{X} = [\boldsymbol{\alpha}, \boldsymbol{\beta}, \boldsymbol{r}, \eta]$ through the vectors `lb` and `up`. We may thus easily impose the constraints (5.7) on the unknown components of the vector $\boldsymbol{X}$. The routine `lsqnonlin` stops when one of the following criteria is met:

- the maximum number of iterations performed (`MaxIter`),
- the maximum number of evaluations of the objective function (`MaxFunEvals`),
- the termination tolerance for the vector of unknowns $\boldsymbol{X}$ (`TolX`),
- the termination tolerance for the objective function value (`TolFun`).

The quantities `MaxIter, MaxFunEvals, TolX, TolFun` are user–prescribed and, in the present study, we took `TolX`=`TolFun`=10^{-14}, `MaxFunEvals`=2×10^6 and controlled the convergence with appropriate values of `MaxIter`. In most cases the process stopped when `MaxIter` was exhausted, but in some instances the tolerance `TolX` was reached. For more details, see, for example, [14, 17].

6. Numerical examples for the inverse problem

Bearing in mind that the obstacles (6.2)-(6.4) that are considered to be retrieved in the sequel are all contained in the unit disk, we choose the location of the measurement curve Γ to be a circle of radius $R_1 = 2.5$ (centred at the origin), which is neither too close nor too far from the unity. Limited aperture data (5.4) taken over an arc Γ, e.g. half of the circle, [21], did not produce accurate results and are therefore not presented.

For the Oseen flow, we took the parameters $\varrho = 1, \mu = 1$ and $\mathrm{U}_\infty = 0.5$ (corresponding to $Re = 1$). The input velocity data (5.4) is numerically simulated by first solving the corresponding direct problem, as described in Sections 2 and 4, with $M = 196$ and $N = 148$. Furthermore, in order to simulate the errors that are inherently present in any practical measurement and to test the stability of the inversion, this data is perturbed by a multiplicative noise as

$$\boldsymbol{\varphi}^{\varepsilon}(\boldsymbol{x}_{\ell+N}) = (1 + \chi\, \mathrm{p})\, \boldsymbol{\varphi}(\boldsymbol{x}_{\ell+N}), \quad \ell = \overline{1, L}, \tag{6.1}$$

where p represents the percentage of noise and χ is a pseudo-random noisy variable drawn from a uniform distribution in [-1, 1] using the MATLAB© command `-1 + 2*rand(1,L)`. When the noisy data (6.1) is inverted, due to the ill-posedness of the inverse obstacle problem, regularization needs to be employed in the functional (5.6). The simultaneous choice of the two regularization parameters could be based on the L-surface criterion, [4, 11], but in this study we choose the regularization parameters λ_1 and λ_2 by taking one to be zero and varying the other by trial and error or by the L-curve analysis [10, 18, 19]. In all examples considered we took $M = N = 20$, $L = 51$ and the initial guesses $\boldsymbol{\alpha}^0 = \boldsymbol{\beta}^0 = \mathbf{0}$ and $\eta^0 = 2/3$. As previously mentioned in Section 5, the number of sensors L giving the $2L$ fluid velocity measurements (5.5) needs to be taken greater than $N/2 = 10$ in order for the functional (5.6) to impose at least the same number of equations as unknowns. Thus, in principle, taking $L = 11$, should suffice. However, after a few numerical trials we have decided to present results for a larger value of L, namely $L = 51$ which produces

numerical reconstructions that do not significantly change under the adoption of a larger value of L.

6.1. **Example 4: Circular obstacle.** In this case the obstacle to be reconstructed is a circle of radius

$$r(\vartheta) = 1, \quad \vartheta \in [0, 2\pi). \tag{6.2}$$

We took $r_{\min} = 0.5$ and $r_{\max} = 1.5$ and the initial guess $\boldsymbol{r}^0 = 0.7$. In Figure 7(a), the convergence of results obtained with no noise and no regularization for different numbers of iterations `niter` is illustrated. In Figures 7(b) and 7(c) we present the plots of the reconstructed boundary for various values of the regularization parameter λ_1 when $\lambda_2 = 0$, and λ_2 when $\lambda_1 = 0$, respectively, and p =5% after 1000 iterations. From these figures it can be seen that regularization with λ_2 which penalizes the smoothness of the shape to be reconstructed is more important than the regularization with λ_1 which is imposed to alleviate the ill-conditioning of the MFS.

6.2. **Example 5: Bean-shaped obstacle.** We next consider the bean-shaped domain [3, 21] with polar radius

$$r(\vartheta) = \frac{1 + 0.9\cos(\vartheta) + 0.1\sin(\vartheta)}{1 + 0.75\cos(\vartheta)}, \quad \vartheta \in [0, 2\pi). \tag{6.3}$$

We took $r_{\min} = 0.1$ and $r_{\max} = 1.5$ and the initial guess $\boldsymbol{r}^0 = 1$. In Figure 8(a) we present the results obtained with no noise and no regularization for different numbers of iterations `niter`. Compared to the smooth circular obstacle (6.2) of the previous example, the bean-shaped domain (6.3) presents a cusp facing the incoming flow which makes the convergence of its reconstruction much slower needing more than around 10000 iterations. In Figures 8(b) and 8(b) we present the plots of the reconstructed boundary for various values of the regularization parameter λ_1 when $\lambda_2 = 0$, and λ_2 when $\lambda_1 = 0$, respectively, and p =1% after 1000 iterations.

6.3. **Example 6: Peanut-shaped obstacle.** We finally consider the peanut-shaped domain [13, 15, 21] described by

$$r(\vartheta) = \sqrt{\cos^2(\vartheta) + 0.25\sin^2(\vartheta)} = \frac{1}{2}\sqrt{1 + 3\cos^2(\vartheta)}, \quad \vartheta \in [0, 2\pi). \tag{6.4}$$

We took $r_{\min} = 0.1$ and $r_{\max} = 1.5$ and the initial guess $\boldsymbol{r}^0 = 1$. Numerical results with or without noise and regularization are presented in Figures 9(a)-9(c) and similar conclusions to those obtained for Example 5 can be derived.

7. Conclusions

In this paper, the MFS has been developed and applied for the solution of both direct and inverse problems for the Oseen flow past arbitrary known or unknown obstacles. The numerically obtained results are in good agreement with those previously reported in the literature for the direct problem. The results obtained for the inverse problems considered yield comparable retrievals to those obtained in [21] for the inverse obstacle problem using a half circle aperture but many fluid velocities obtained by sending the fluid flow at five different angles inclined to the horizontal. The MFS has further potential for the solution of three-dimensional such Oseen flow problems. Future work will be concerned with solving the interior Oseen obstacle problem where the star-shaped (soft/rigid inclusion) obstacle Ω has to be reconstructed from the measurement of the fluid velocity on $\Gamma = \partial B(\mathbf{0}; R_1)$ and the stress force (fluid traction) $\boldsymbol{t}$ on $\Gamma_1 \subset \Gamma$, [1], or ∇p on Γ_1, [7].

Acknowledgements

The authors are grateful to the University of Cyprus for supporting this research and also wish to thank Dr Fotos Stylianou of the University of Cyprus for his help and advice.

References

[1] C. Alvarez, C. Conca, L. Friz, O. Kavian and J. H. Ortega, *Identification of immersed obstacles via boundary measurements*, Inverse Problems **21** (2005), 1531–1552.
[2] C. J. S. Alves and A. L. Silvestre, *Density results using Stokeslets and a method of fundamental solutions for the Stokes equations*, Eng. Anal. Boundary Elements **28** (2004), 1245–1252.
[3] C. J. S. Alves, R. Kress and A. L. Silvestre, *Integral equations for an inverse boundary value problem for the two-dimensional Stokes equations*, J. Inverse Ill-Posed Probl. **15** (2007), 461–481.
[4] M. Belge, M. Kilmer and E. L. Miller, *Efficient determination of multiple regularization parameters in a generalized L-curve framework*, Inverse Problems **18** (2002), 1161–1183.
[5] M. B. Bush, *Modelling two-dimensional flow past arbitrary cylindrical bodies using boundary element formulations*, Appl. Math. Modelling **7** (1983), 386–394.
[6] C. W. Chen, D. L. Young, C. C. Tsai and K. Murugesan, *The method of fundamental solutions for inverse 2D Stokes problems*, Comput. Mech. **37** (2005), 2–14.
[7] A. Doubova, E. Fernandez-Cara and J. H. Ortega, *On the identification of a single body immersed in a Navier-Stokes fluid*, European J. Appl. Math. **18** (2007), 57–80.
[8] C. Fabre and G. Lebeau, *Prolongement unique des solutions de l'equation de Stokes*, Comm. Partial Differential Equations **21** (1996), 573–596.
[9] H. Fujikawa, *The forces acting on two circular cylinders of arbitrary radii placed in a uniform stream at low values of Reynolds number*, J. Phys. Soc. Japan **11** (1956), 690–701.
[10] P. C. Hansen, The L-curve and its use in the numerical treatment of inverse problems. In: Computational Inverse Problems in Electrocardiology (ed. P. Johnston), WIT Press, Southampton, pp. 119-142 (2001).
[11] A. Hazanee and D. Lesnic, *Reconstruction of an additive space- and time-dependent heat source*, Eur. J. Comput. Mech. **22** (2013), 304–329.
[12] I. Imai, *A new method of solving Oseen's equations and its application to the flow past an inclined elliptic cylinder*, Proc. Roy. Soc. London. Ser. A. **224** (1954), 141–160.
[13] O. Ivanyshyn, *Shape reconstruction of acoustic obstacles from the modulus of the far field pattern*, Inverse Probl and Imaging **1** (2007), 609–622.

[14] M. A. Jankowska, A. Karageorghis and C. S. Chen, *Improved Kansa RBF method for the solution of nonlinear boundary value problems*, Eng. Anal. Boundary Elements **87** (2018), 173–183.
[15] A. Karageorghis and D. Lesnic, *Application of the MFS to inverse obstacle scattering problems*, Eng. Anal. Boundary Elements **35** (2011), 631–638.
[16] A. Karageorghis, D. Lesnic, and L. Marin, *A survey of applications of the MFS to inverse problems*, Inverse Probl. Sci. Eng. **19** (2011), 309–336.
[17] A. Karageorghis, D. Lesnic and L. Marin, *A moving pseudo-boundary method of fundamental solutions for void detection*, Numer Methods Partial Differential Eq **29** (2013), 935–960.
[18] A. Karageorghis, D. Lesnic and L. Marin, *The method of fundamental solutions for three-dimensional inverse geometric elasticity problems*, Computers and Structures **166** (2016), 51–59.
[19] A. Karageorghis, D. Lesnic and L. Marin, *The plane waves method for numerical boundary identification*, Adv. Appl. Math. Mech. **9** (2017), 1312–1329.
[20] M. A. Kelmanson, *A direct boundary integral equation formulation for the Oseen flow past a two-dimensional cylinder of arbitrary cross-section*, Acta Mech. **68** (1987), 99–119.
[21] R. Kress and S. Meyer, *An inverse boundary value problem for the Oseen equation*, Math. Meth. Appl. Sci. **23** (2000), 103–120.
[22] The MathWorks, Inc., 3 Apple Hill Dr., Natick, MA, *Matlab*.
[23] K. Nishida, *Numerical method for Oseen's linearized equations in three-dimensional exterior domains*, J. Comput. Appl. Math. **152** (2003), 405–409.
[24] P. A. Ramachandran, *Method of fundamental solutions: singular value decomposition analysis*, Commun. Numer. Meth. Engng **18** (2002), 789–801.
[25] S. Tomokita and T. Aoi, *The steady flow of viscous fluid past a sphere and circular cylinder at small Reynolds numbers*, Quart. J. Mech. Appl. Math. **3** (1950), 141–161.
[26] S. Tomokita and T. Aoi, *An expansion formula for the drag on a circular cylinder moving through a viscous fluid at small Reynolds numbers*, Quart. J. Mech. Appl. Math. **4** (1951), 401–406.
[27] W. Wang and P. H. Wen, *Interaction between micro-particles in Oseen flows by the method of fundamental solutions*, Eng. Anal. Boundary Elements **32** (2008), 318–327.
[28] H. Yano and A. Kieda, *An approximate method for solving two-dimensional low-Reynolds-number flow past arbitrary cylindrical bodies*, J. Fluid Mech. **97** (1980), 157–179.
[29] D. L. Young, S. J. Jane, C. M. Fan, K. Murugesan and C. C. Tsai, *The method of fundamental solutions for 2D and 3D Stokes problems*, J. Comput. Phys. **211** (2006), 1–8.

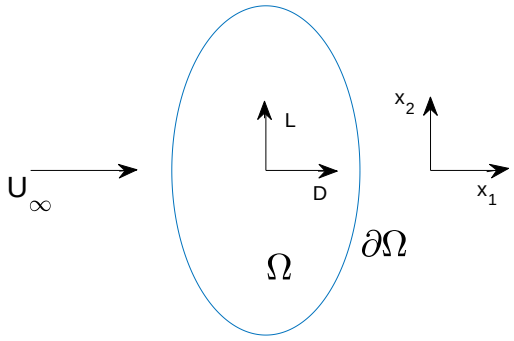

FIGURE 1. Flow past an arbitrary body Ω showing directions of positive drag (D) and lift (L).

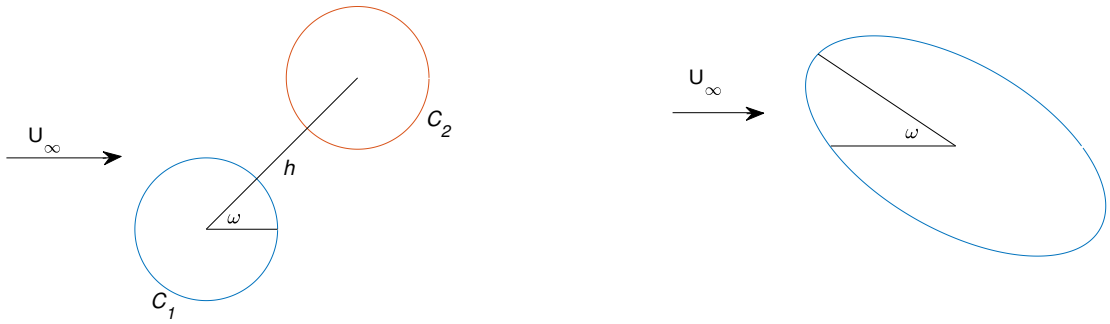

(a) (b)

FIGURE 2. Geometry of (a) Example 2 and (b) Example 3.

DEPARTMENT OF MATHEMATICS AND STATISTICS, UNIVERSITY OF CYPRUS/ ΠΑΝΕΠΙΣΤΗΜΙΟ ΚΥΠΡΟΥ, P.O.BOX 20537, 1678 NICOSIA/ΛΕΥΚΩΣΙΑ, CYPRUS/ΚΥΠΡΟΣ
E-mail address: andreask@ucy.ac.cy

DEPARTMENT OF APPLIED MATHEMATICS, UNIVERSITY OF LEEDS, LEEDS LS2 9JT, UK
E-mail address: amt5ld@maths.leeds.ac.uk

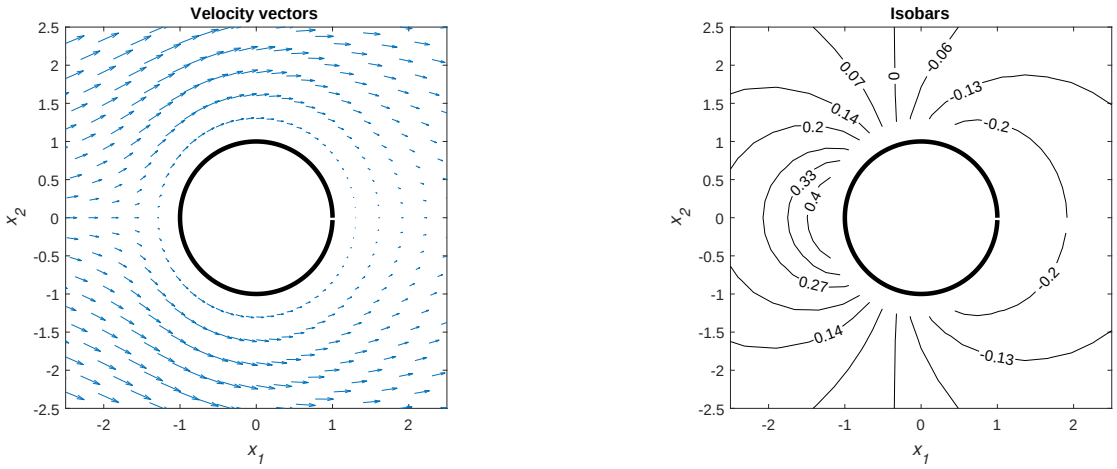

(a) (b)

FIGURE 3. Example 1: (a) Velocity vectors and (b) Lines of constant pressure (isobars) for $Re = 1$.

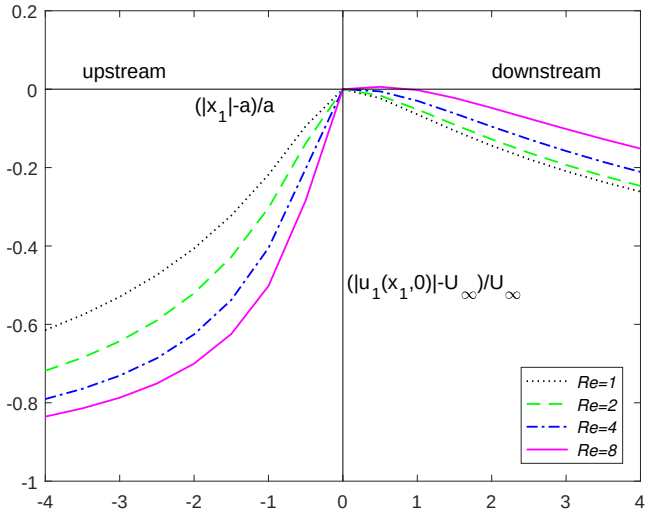

FIGURE 4. Example 1: Dimensionless fluid velocity $\dfrac{|u_1(x_1,0)| - \mathrm{U}_\infty}{\mathrm{U}_\infty}$ on the line of symmetry (centreline), as a function of the distance $\dfrac{|x_1| - a}{a}$, for various Reynolds numbers.

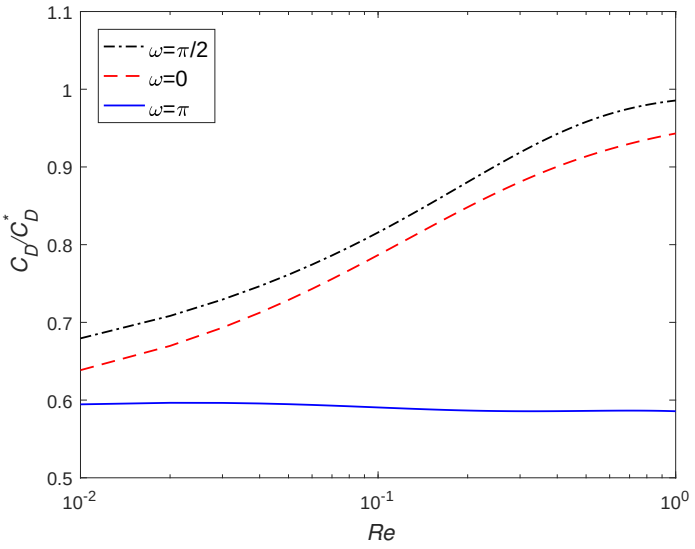

(a)

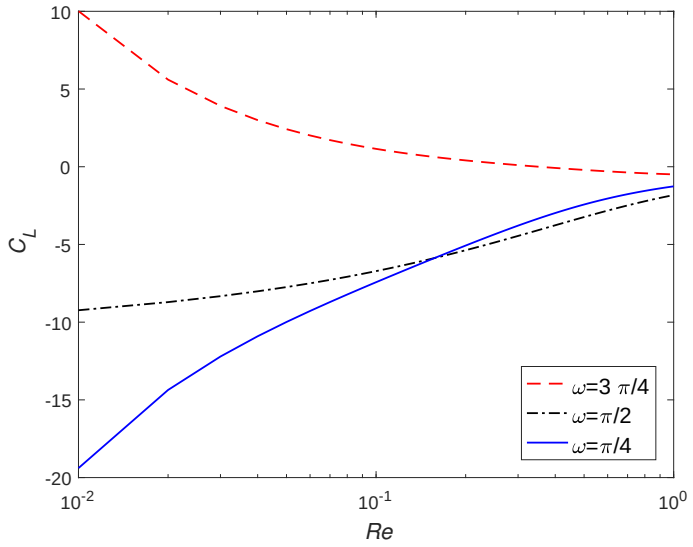

(b)

FIGURE 5. Example 2: (a) Ratio C_D/C_D^* on cylinder C_1 and (b) coefficient C_L on cylinder C_1 versus the Reynolds number Re.

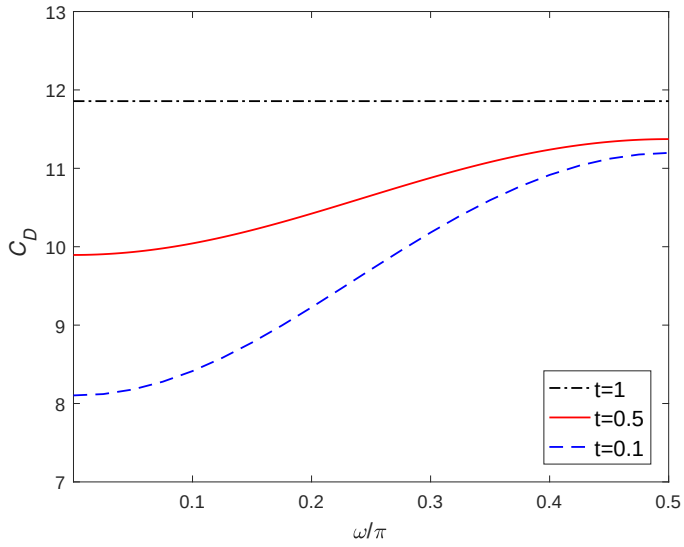

(a)

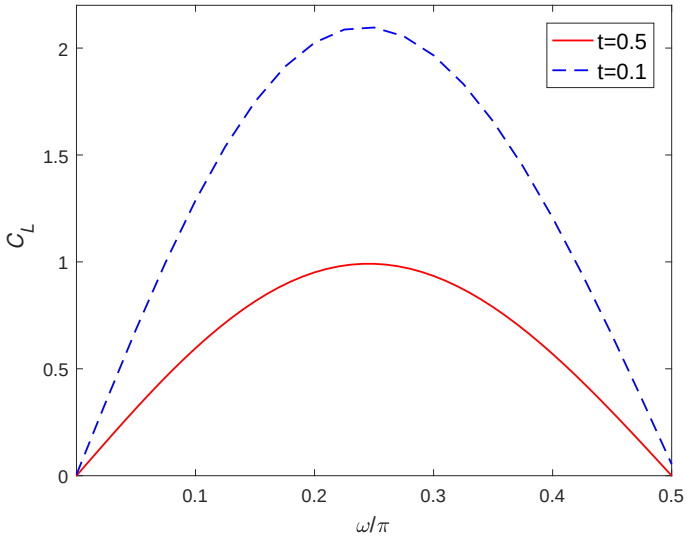

(b)

FIGURE 6. Example 3: (a) Coefficient C_D and (b) coefficient C_L versus the angle ω.

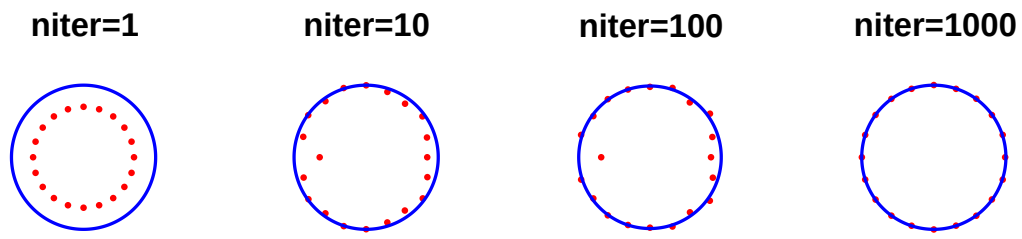

(a)

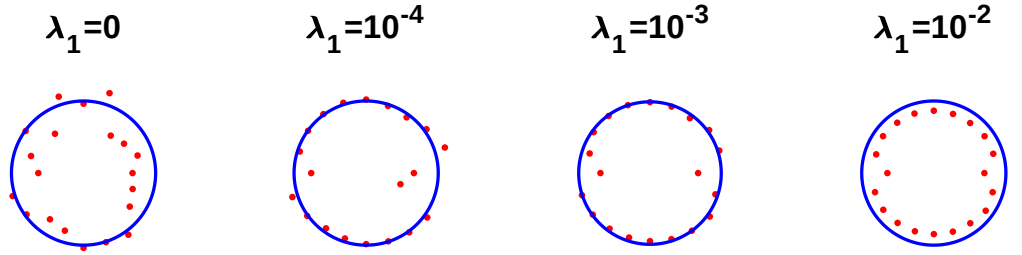

(b)

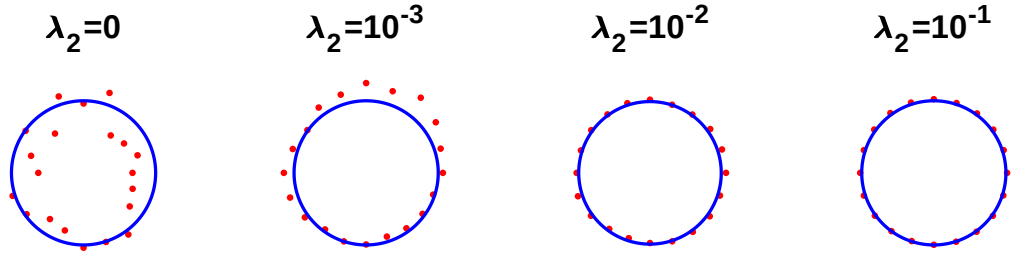

(c)

FIGURE 7. Example 4: Results (a) with no noise and no regularization, (b) for various values of λ_1, p = 5% noise, and $\lambda_2 = 0$, (c) for various values of λ_2, p = 5% noise, and $\lambda_1 = 0$.

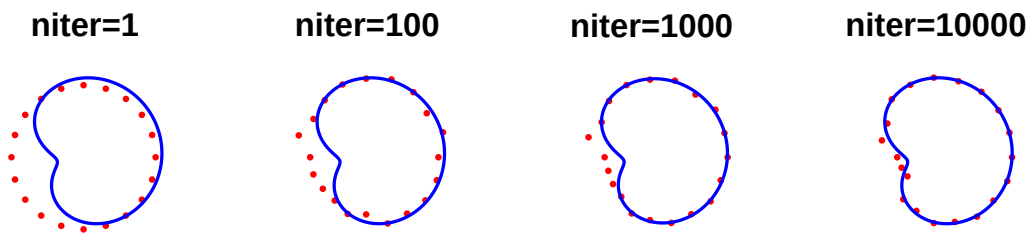

(a)

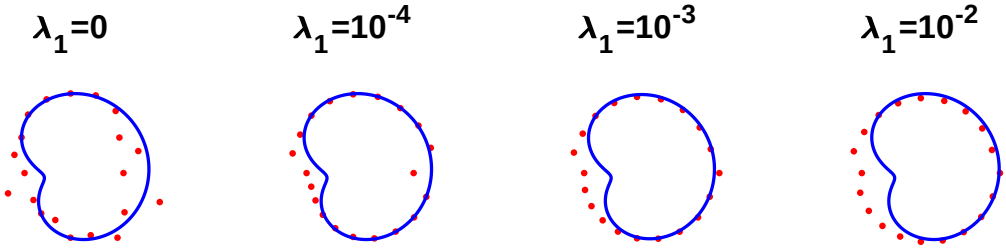

(b)

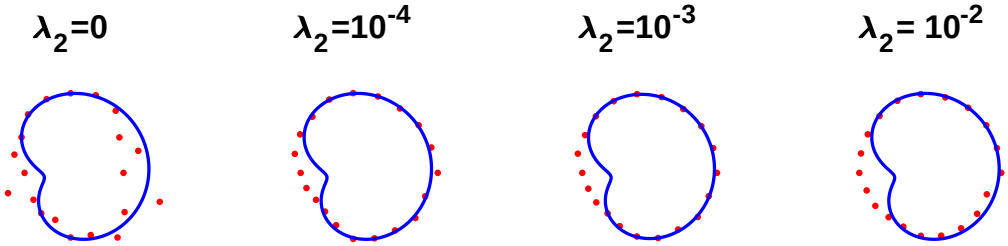

(c)

FIGURE 8. Example 5: Results (a) with no noise and no regularization, (b) for various values of λ_1, p = 1% noise, and $\lambda_2 = 0$, (c) for various values of λ_2, p = 1% noise, and $\lambda_1 = 0$.

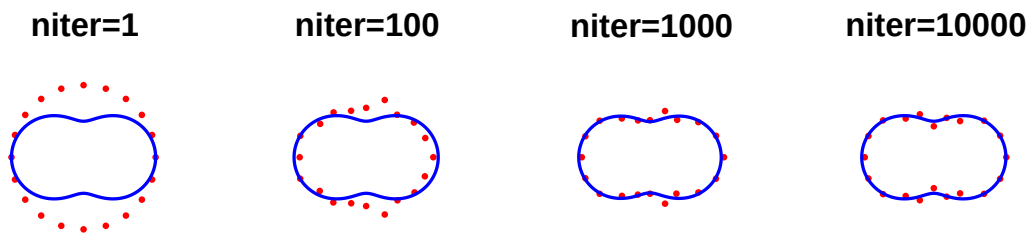

(a)

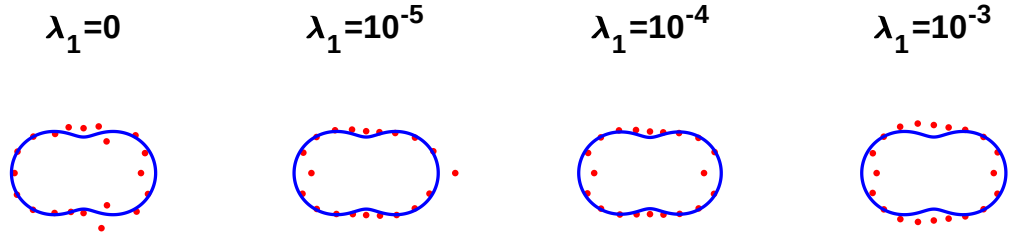

(b)

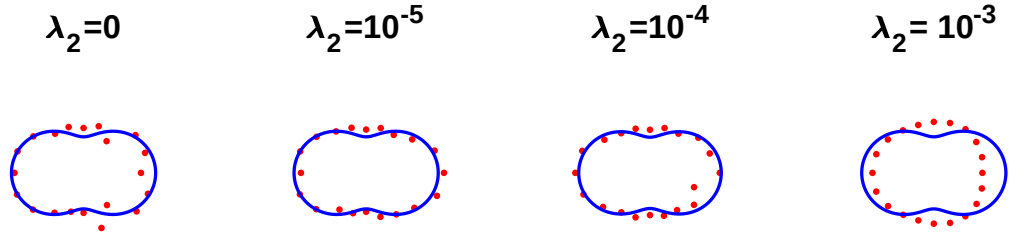

(c)

FIGURE 9. Example 6: Results (a) with no noise and no regularization, (b) for various values of λ_1, p = 1% noise, and $\lambda_2 = 0$, (c) for various values of λ_2, p = 1% noise, and $\lambda_1 = 0$.